TRANSIENT MODEL FOR SURGE AND SWAB PRESSURES IN WELL DRILLING

Fernando Thadeu G. M. C. de Almeida, fernandoalmeida@utfpr.edu.br
Thiago Bruno de Matos, thiago.brunomatos@gmail.com
Cezar Otaviano R. Negrão, negrao@utfpr.edu.br
Silvio Luiz M. Junqueira, sivio@utfpr.edu.br
Laboratório de Ciências Térmicas – LACIT, Universidade Tecnológica Federal do Paraná – UTFPR, Curitiba – PR 80230-901

André Leibsohn Martins, aleibsohn@petrobras.com.br
Roni Abensur Gandelman, roniag@petrobras.com.br
Tecnologia de Engenharia de Poço – TEP, Centro de Pesquisa da PETROBRAS - CENPES, Rio de Janeiro-RJ 21941-915

Abstract. *The axial movement of drill pipes is a common operation in oil well drilling. This motion displaces the drilling fluid and causes pressure changes in the borehole. The descending pipe movement increases the pressure at the bottom hole (surge) and its extraction reduces it (swab). If the bottom hole pressure overcomes the formation fracture pressure, circulation loss may take place. On the other hand, if the pressure within the well is smaller than the pore pressure, kicks can occur. In order to maintain the bottom hole pressure within the formation fracture and pore pressures, the drill pipe must be moved slowly and therefore, the task becomes quite time consuming. The current work presents a mathematical model to predict surge and swab pressures in annular spaces. The approach is based on conservation equations of mass and momentum. The fluid flow is considered laminar, one-dimensional, compressible, isothermal and transient. The fluid is regarded firstly as Newtonian and afterwards as a Power Law fluid, in both cases with constant compressibility. The viscous effect is lumped and the concept of friction factor is applied. The governing differential equations are non-linear and therefore, they are solved numerically by the finite volume method. A sensitivity analysis of the flow parameters is carried out. For instance, the pressure wave propagation is observed for low compressibility fluids. Pressure oscillation is observed for low aspect ratio ratios and low Power Law indexes.*

Keywords*: Couette flow, Surge Swab, Unsteady Flow, Power Law Fluid*

1. INTRODUCTION

Axial drill pipe displacement causes drilling fluid flow through annular space between the borehole and drill pipe. A pressure increase known as surge is observed while the drill pipe is introduced into the well borehole. The pressure, however, cannot be higher than the formation fracture pressure otherwise circulation loss can occur. On the other hand, the extraction of the drill pipe produces low pressures (swab) at the borehole which cannot be lower than the pore pressure in order to avoid formation fluid flow into the well. Therefore, the predictions of surge and swab pressures are important to determinate adequate conditions to prevent circulation losses and kicks.

Several models have been developed to predict surge and swab pressures. Those models are based on conservation equations of mass and momentum and on the constitutive equations for Bingham and Power law fluids. The models found in literature can be divided into steady and unsteady. Steady state models developed by Burkhardt (1964), Fontenot and Clark (1974), Yang and Chuckwu (1995) and Bing *et al.* (1995) evaluates surge and swab pressures by considering only the viscous effects. Bing and Kaiji (1996), Lal (1983) and Wang and Chuckwu (1996) are examples of unsteady state models. These models are capable to predict both viscous and inertial effects. As the drilling fluid flow is transient, the unsteady state models should be more appropriate the steady state ones.

The current work presents a mathematical model to predict pressures caused by the axial drill pipe motion. The flow is modeled by the conservation equations of mass and momentum which are numerically solved by the finite volume method. A parametric analysis is carried out to investigate the effects of dimensionless parameters.

2. MATHEMATICAL MODEL

Figure 1 illustrates the downward motion of drill pipe, with velocity V_p, displacing the drilling fluid flow through the annular space. The borehole wall is represented by the external surface of diameter D_h, and the drill pipe corresponds to the internal cylinder of diameter D_p. The pipe runs with velocity V_p creating a pressure gradient that moves the fluid out of the hole. However, some the fluid is dragged by the drill pipe due to friction. One can see the problem can be approximated by the axial Couette flow under pressure gradient between two cylindrical surfaces.

The transient flow is assumed to be laminar, isothermal and homogeneous one-dimensional. Fluid compressibility is considered constant and the wall viscous drag is lumped at the walls. The drill pipe is closed and the cross-sectional area of the annular is space is uniform. Therefore the flow domain is an annular space of length L, internal diameter D_p and external diameter D_h. Elastic deformation and gravitational effects are neglected.

2.1. Governing Equations

The first governing equation is obtained by applying a mass balance to a control volume in the annular region:

$$\frac{\partial \left(\rho \bar{V} \right)}{\partial z} + \frac{\partial \rho}{\partial t} = 0 \tag{1}$$

where ρ and $\bar{V}$ are, respectively, the density and average velocity. t and z are the time and axial position, respectively.
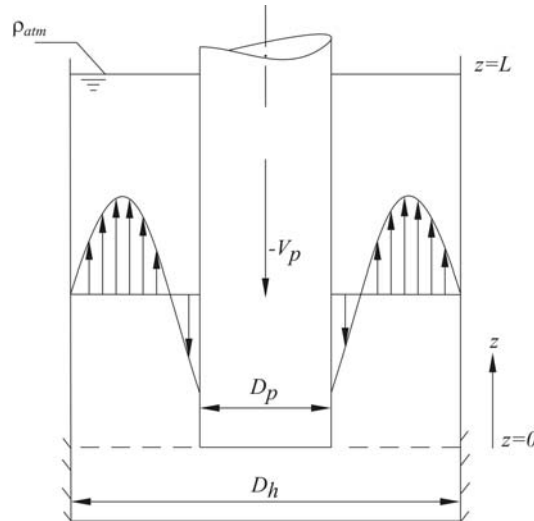

Figure 1 – Velocity profile in an annular space.

The momentum balance applied to the annular space is the second governing equation.

$$\frac{\partial \left(\rho \bar{V} \right)}{\partial t} + \frac{\partial \left(\rho \bar{V} \bar{V} \right)}{\partial z} = -\frac{\partial P}{\partial z} + \frac{\pi}{A_t} \left(D_h \tau_h - D_p \tau_p \right) \tag{2}$$

where τ_h and τ_p are the shear stresses at the external and internal walls, respectively, and A_t is the annular cross-sectional area.

The evaluation of the friction effects are closely related to the model of non-Newtonian fluid considered here. For Newtonian fluids the following equation for shear stress is employed:

$$\tau = \mu \dot{\gamma} \tag{3}$$

where μ is the viscosity and $\dot{\gamma}$ is the strain ratio.

On the other hand, for Power Law fluids the shear stress is not directly proportional to the strain ratio. In this case, the following equation is used:

$$\tau = \mu \left(\dot{\gamma} \right)^n \tag{4}$$

where n is the Power Law index.

Assuming an isothermal flow and a constant fluid compressibility, the pressure can be found by (Kimura, 2008):

$$P = P_{atm} + \frac{1}{\alpha} \ln \left(\frac{\rho}{\rho_{atm}} \right) \tag{5}$$

where P is the fluid pressure, α is the fluid compressibility and ρ is the density. The index *atm* indicates the atmospheric condition.

Initially, the flow is at rest, the fluid is under the atmospheric pressure and the fluid density within the whole domain is ρ_{atm}. The initial conditions are thus written as:

$$\bar{V}(z, t = 0) = 0 \tag{6}$$

$$\rho(z, t = 0) = \rho_{atm} \tag{7}$$

The volumetric rate displaced by the pipe is assumed to be totally pushed through the annular space and therefore, the flow velocity at the bottom of the well (inlet velocity) is defined by:

$$\bar{V}(z = 0, t) = \frac{A_p}{A_t} V_p \tag{8}$$

where A_p is pipe the sectional cross area.

Since the ρ_{atm} is a known and constant value at the upper boundary, the continuity Eq. (1) can be written as the second boundary condition:

$$\left. \frac{\partial(\rho\bar{V})}{\partial z} \right|_{z=L} = 0 \tag{9}$$

3. METHODOLOGY OF SOLUTION

The solution of Eqs. (1), (2) and (5) provides the velocity, density and pressure fields. Initial and boundary conditions, expressed by Eqs. (6), (7), (8) and (9), are necessary to solve Eqs. (1) and (2). Since Eq. (2) is a nonlinear equation, there is not a solution for the system. For this reason, the set of equations was solved numerically by the finite volume method (Versteeg and Malalasekera, 1995).

A uniform staggered grid is employed. The velocities are placed at the faces of the scalar variable (ρ and P) cells. The governing Eqs. (1) and (2) are discretized by the Finite Volume Method and a set of algebraic equations arises. The algebraic continuity and momentum equation are solved iteratively for density and velocity, respectively. The pressure is obtained from the Equation of state (5). The convergence criterion is based on the mass and momentum conservation equations:

$$\frac{\sum_{i=1}^{n}(\rho\bar{V})_i}{(\rho\bar{V})_1} \cdot 100 < e \tag{10}$$

$$\frac{\sum_{i=1}^{n}(\rho\bar{V}\bar{V})_i}{(\rho\bar{V}\bar{V})_1} \cdot 100 < e \tag{11}$$

where e is the convergence criterion, n is the number of finite volumes and index 1 identifies the first control volume. Convergence is reached when residues of mass (Eq. (9)) and momentum (Eq. (10)) are lower than e.

4. RESULTS

In order to reduce the number of parameters the problem results were normalized according to the variables and parameters defined in Tab. 1 and 2.

4.1. Numerical Model Evaluation

The sensitivity to the grid size and to the convergence criterion was firstly conducted. For such analysis, a reference case was established. The reference values were $\alpha^*=1.27\times10^{-5}$, $RA=10^6/3$, $Re=400$ and $y=0.4$. Because of the hyperbolic characteristic of the governing equations the time and space grid sizes have to satisfy the Courant-Friedrichs-Lewy

(*CFL*) stability criterion (Fortuna, 2000). The *CFL* criterion establishes that the ratio of space and time grid sizes must be smaller than or equal to the pressure wave speed. In all simulations, this ratio was equal to half of the wave speed.

Figure 2 shows the effect of the convergence criterion on the pressure field at a specific time. One can see the solution becomes convergence criterion independent for e=1%. To check the sensitivity of the results to number of finite volumes, three numbers of grid cells were tested: 100, 200 and 400 volumes. Although the pressure field is almost insensitive to these three grids the velocity field becomes insensitive to 200 finite volumes, as shown in Fig. 3. Therefore, 200 volume grid will be used for the results shown below.

<table>
<tr><th colspan="2">Table 1 – Dimensionless variables.</th><th colspan="2">Table 2 – Dimensionless groups identified.</th></tr>
<tr><td>Dimensionless Variable</td><td>Definition</td><td>Dimensionless Group</td><td>Definition</td></tr>
<tr><td>Pressure</td><td>$\dfrac{P - P_{atm}}{\rho_{atm} V_p^2}$</td><td>Aspect ratio</td><td>$RA = \dfrac{L}{\left(D_h - D_p\right)}$</td></tr>
<tr><td>Density</td><td>$\rho^* = \dfrac{\rho}{\rho_{atm}}$</td><td>Reynolds number</td><td>$Re = \dfrac{\rho_{atm} V_p \left(D_h - D_p\right)}{\mu}$</td></tr>
<tr><td>Average Velocity</td><td>$V^* = \dfrac{\overline{V}}{V_p}$</td><td>Dimensionless Compressibility</td><td>$\alpha^* = \alpha \rho_{atm} V_p^2$</td></tr>
<tr><td>Time</td><td>$t^* = t\dfrac{V_p}{L}$</td><td>Diameter ratio</td><td>$y = \dfrac{D_p}{D_h}$</td></tr>
<tr><td>Position</td><td>$Z^* = \dfrac{z}{L}$</td><td></td><td></td></tr>
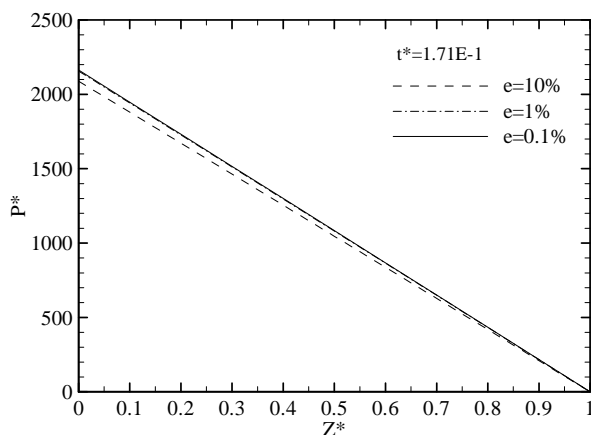</table>

Figure 2 – Pressure field at steady state for different convergence criteria.
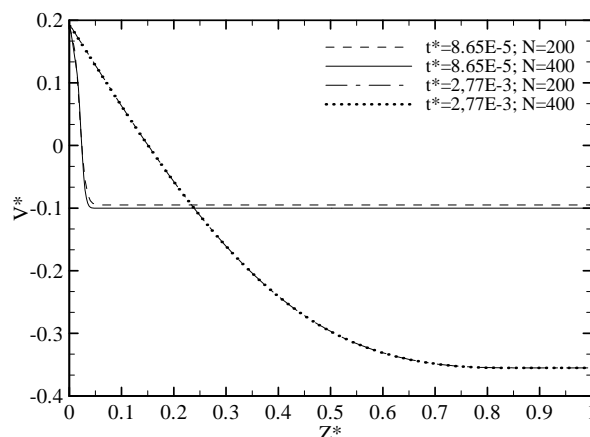

Figure 3 – Velocity field for different grids.

4.2. Parametric Analysis

The effect of the diameter ratio was evaluated carrying out tests for *y*=0.2, *y*=0.4 and *y*=0.8. The other dimensionless parameters were maintained constant at the following values: α^*=1.27×10^{-5}, *Re*=400 e *RA*=10^6/3. Figure 4 illustrates velocity field for various time and *y*=0.8. The curves 1 and 2, in Fig. 4, are the velocity field at the first time step and the steady state, respectivelly.
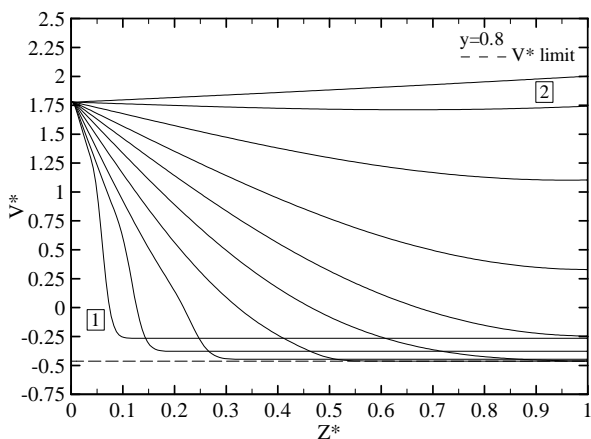
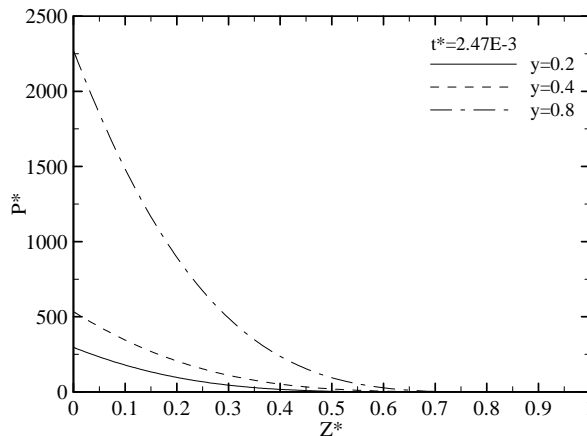Figure 4 – Velocity field for various times and *y*=0.8.

Figure 5 – Pressure field at t*=2.47x10⁻³ for three diameter ratios.

At the inlet the dimensionless velocity is kept constant (1.75) for the whole simulation. At the beginning of the flow (curve 1), the velocity drops to -0.25 at z*=0.1 and is kept constant up to the pipe outlet. As the fluid is dragged by the drill pipe the velocity assume negative values at the start-up. The dashed line indicates the velocity for a zero pressure gradient Couette flow and that is the lowest velocity reached. As time evolves the pressure effect overcomes the viscous drag and the whole velocity field becomes positive. Although the steady state has been achieved the velocity increases from the inlet to the outlet, as shown in Fig. 2. The reason for that is the decrease of the density from the inlet to the outlet, as the pressure decreases.

The limit velocity at which fluid is dragged can be developed considering a Couette flow with no pressure gradient. Considering a steady state flow between cylindrical surfaces, V^*_{limit} is calculated by (White, 1999):

$$V^*_{\lim it} = \frac{1}{2\ln y} + \frac{y^2}{1-y^2} \qquad (12)$$

According to Eq. (12), the higher the diameter ratio the higher the velocity limit. Figure 5 presents the pressure field for different diameter ratios at a fixed time. As expected, the pressure gradient increases as the annular space decreases (higher *y*).

The effect of the Reynolds number was evaluated by fixing the other dimensionless parameters at the following values: $\alpha^*=1.27\times10^{-5}$, $RA=10^6/3$ and *y*=0.4. Figures 6 and 7 illustrate, respectively, the velocity and pressure fields for several Reynolds numbers at $t^*=2.77\times10^{-3}$.
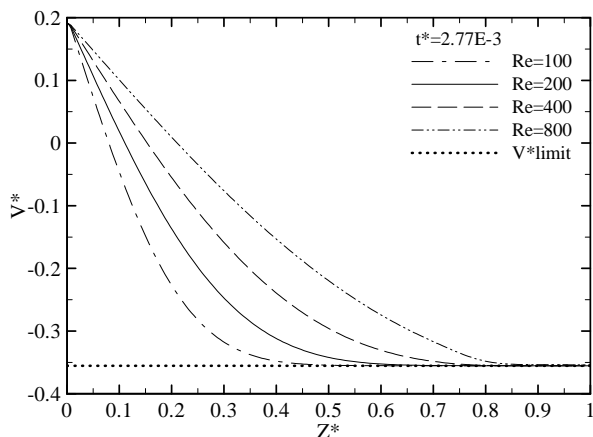

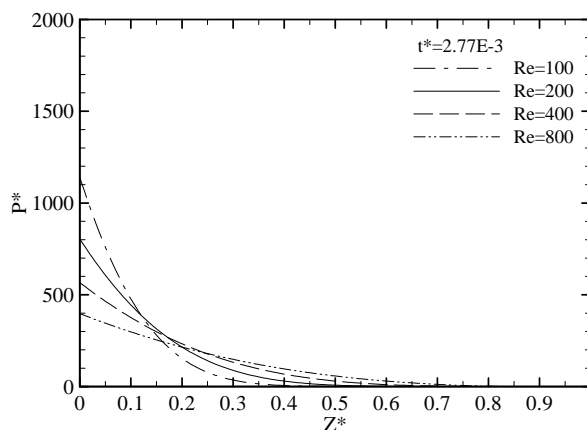Figure 6 – Velocity field for several Reynolds numbers.

Figure 7 – Pressure field for several Reynolds numbers.

According to Fig. 6, the fluid near the outlet ($Z^*=1$) is dragged by the drill pipe and flows in the opposite direction of the pressure driven flow. As the Reynolds number increases the velocity increases in most part of the domain. Additionally, Fig. 7 shows that an increase in Reynolds number decreases the fluid pressure near the inlet ($Z^*=0$). This is expected as the definition of the dimensionless pressure is similar to the friction factor, which as also decreases with the Reynolds number. On the other hand, the higher the Reynolds number the larger the region affected by the pressure.

It was also noted that lower the Reynolds number the larger the time for the steady state to be reached. *Re* reduction expands the steady state time.

Figure 8 illustrates pressure field for three compressibility values. Note that, for $\alpha^*=1.27\times10^{-6}$, the pressure wave has reached the outlet of the annular space at $t^*=2.77\times10^{-3}$. For $\alpha^*=1.27\times10^{-4}$ and $\alpha^*=1.27\times10^{-5}$, though, the time was not enough for the pressure wave to move from the inlet to the outlet. Therefore, the lower the compressibility the faster the pressure wave, as the pressure wave is given by $c=1/(\alpha\rho)^{1/2}$ (Anderson, 1990).

Figure 9 shows the pressure field for several times, evolving from curve 1. Curve 1 shows two distinct pressure gradients. The left hand side gradient is defined by the viscous effect and right hand side one is mainly brought about by the pressure wave propagation. Although the intensity of the right hand side gradient has decreased, the two pressure gradients can still be seen in curves 2 and 3. As the time elapses, the position of the pressure wave becomes less evident. This takes place because the viscous effect increases in the pressure wave propagation region. From curve 5 on, the pressure wave has reached the outlet and because of the boundary condition its value does not change at that position, although the pressure gradient continues to increase.
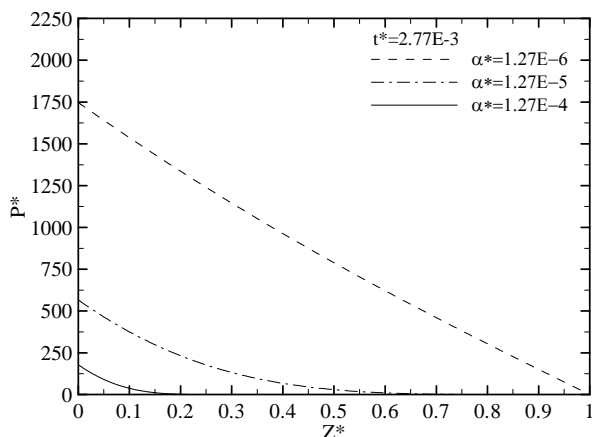

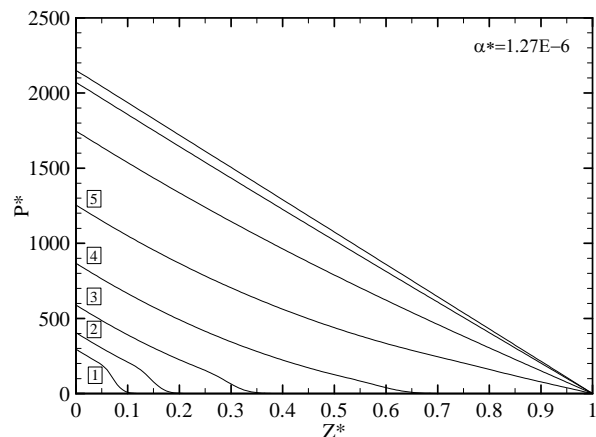Figure 8 – Pressure field for different Dimensionless Compressibilities.

Figure 9 – Pressure field propagation for $\alpha^*=1.27\times10^{-6}$.

The time variation of pressure, for several aspect ratios (*RA*), is presented in Fig. 10. The higher the aspect ratio, the higher the pressure values and the higher the time for the pressure to reach the steady state. Note that the results for *AR*=6200 and *AR*=2500 present pressure oscillations, which the maximum values overcome the steady state values. The lower the aspect ratio, the higher the pressure peaks. Figure 11 also shows the oscillations in the velocity field. The higher the aspect ratio, the closer the minimum velocity is to the Couette flow limit velocity.

The evaluation of the pressure field with time helps to understand the pressure oscillation. Figure 12 presents the pressure field for several times (one for each time-step) and *AR*=2500. The square marked curved is the pressure field at the time the pressure wave reaches the outlet. This curve shows a very steep pressure gradient at the outlet. Figure 13, on the other hand, shows the same squared marked curve and the pressure fields for the subsequent time-steps. The pressure wave is clearly reflected at the outlet boundary at the time $t^*=3.5\times10^{-3}$. Note that the pressure peak at the position $Z^*=0$ (Fig. 14) takes place at the time $t^*=6.9\times10^{-3}$ which is twice the time the pressure wave reaches the outlet. In other words, the pressure wave is now reflected at the inlet. Three other reflections take place later.
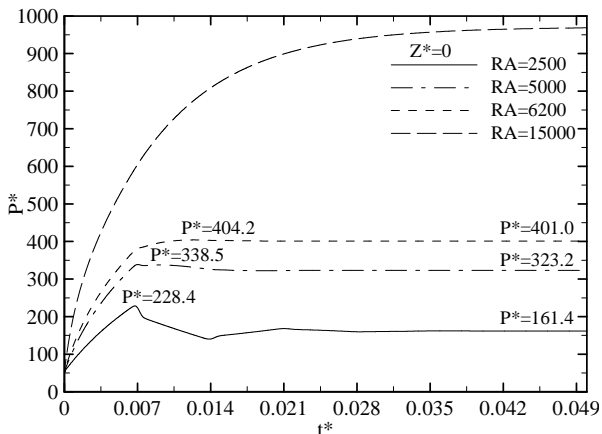
Figure 10 – Time variation of pressure for several aspect ratios at Z^*=0.
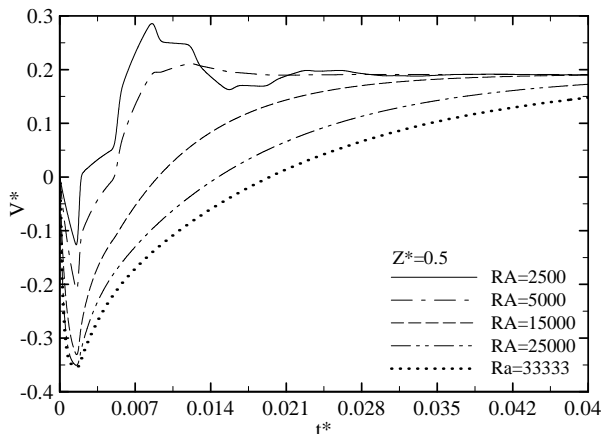

Figure 11 – Time variation of velocity for several aspect ratios at Z^*=0.5.

At the time t*=1.05×10⁻², the wave reaches the outlet boundary for the second time and goes through another reflection. Then, the pressure wave arrives at the left boundary at t*=1.4×10⁻². The reflections cause the oscillation of the pressure which is dumped as the time elapses.

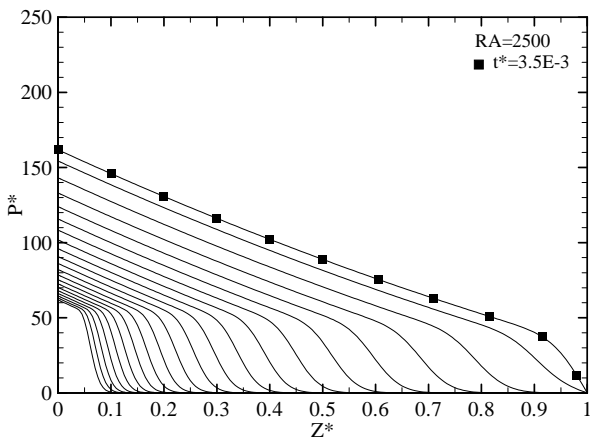

Figure 12 – Pressure field for several time-steps, from t^*=0 to t^*=3.5×10⁻³.

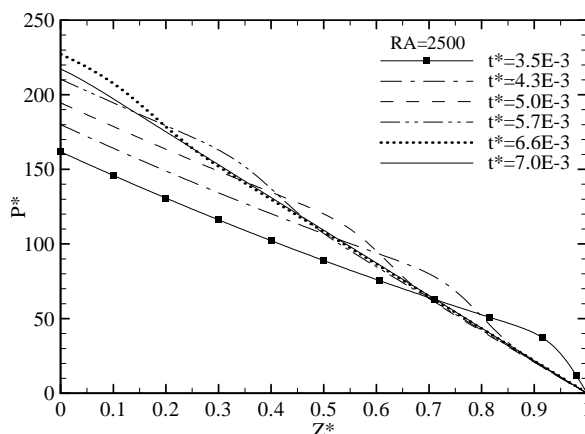Figure 13 – Pressure field for several time-steps, from t^*=3.5×10⁻³ to t^*=7.0×10⁻³.
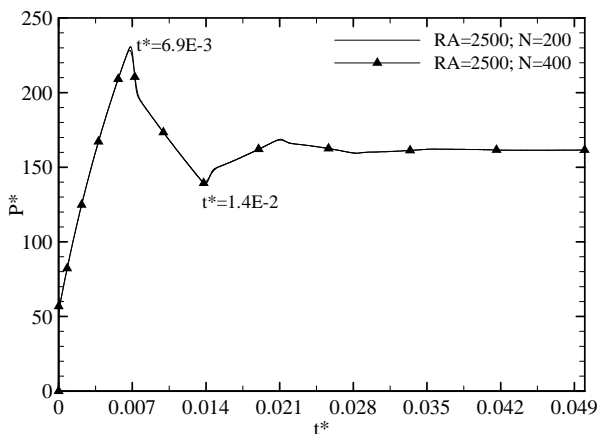

Figure 14 – Time variation of pressure for aspect ratio AR=2500.

The effects of the Power Law index were evaluated by fixing the parameters at α^*=1.27×10⁻⁵, RA=10⁶/3 and y=0.6. Figure 15 shows the time variation of pressure for four different Power Law indexes: 0.4, 0.6, 0.8 and 1.0.
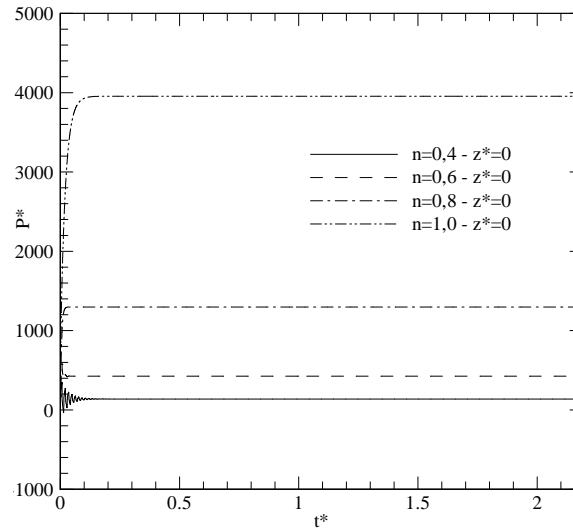
Figure 15 – Time variation of pressure for several Power Law indexes at Z*=0.

Note that the steady state pressure increases when the Power Law index is increased. This behavior can be explained since the pressures losses are greater when the friction effects are more pronounced. It can also be noticed that for low Power Law indexes, namely 0.4 and 0.6, there is pressure oscillation in the beginning of the process. Such oscillation occurs because the friction effects are smaller than in the other cases, and therefore the energy dissipation is also smaller. It is possible to show that these oscillations are due to the wave reflection.

At last, an analysis regarding variations of the drillpipe velocity was performed. For this study it was necessary to compare time and distance in each case, and because of that dimensional results were considered. The dimensional parameters were fixed according to the values shown in Table 3. The fluid was considered as Newtonian.

Table 3 – Dimensional parameters values

Dimensional Parameter	Value
Well Diameter	0,2159 [m] – 8,5 [pol]
Drillpipe Diameter	0,1143 [m] - 4,5 [pol]
Specific Mass	1461,9 [kg/m³]
Viscosity	0,2758 [Pa·s]
Compressibility	$2 \cdot 10^{-9}$ [Pa^{-1}]
Length	5575 [m]

Six different situations were analyzed, two of them with constant drillpipe speed (0.5 and 1.0 m/s). The other four cases are presented in Figure 16.
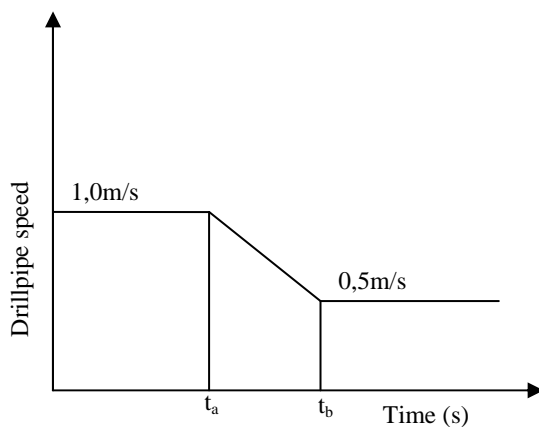
Case	t_a	t_b
3	5s	5s
4	5s	15s
5	15s	25s
6	10s	20s

Figure 16 – Variations in drillpipe velocity

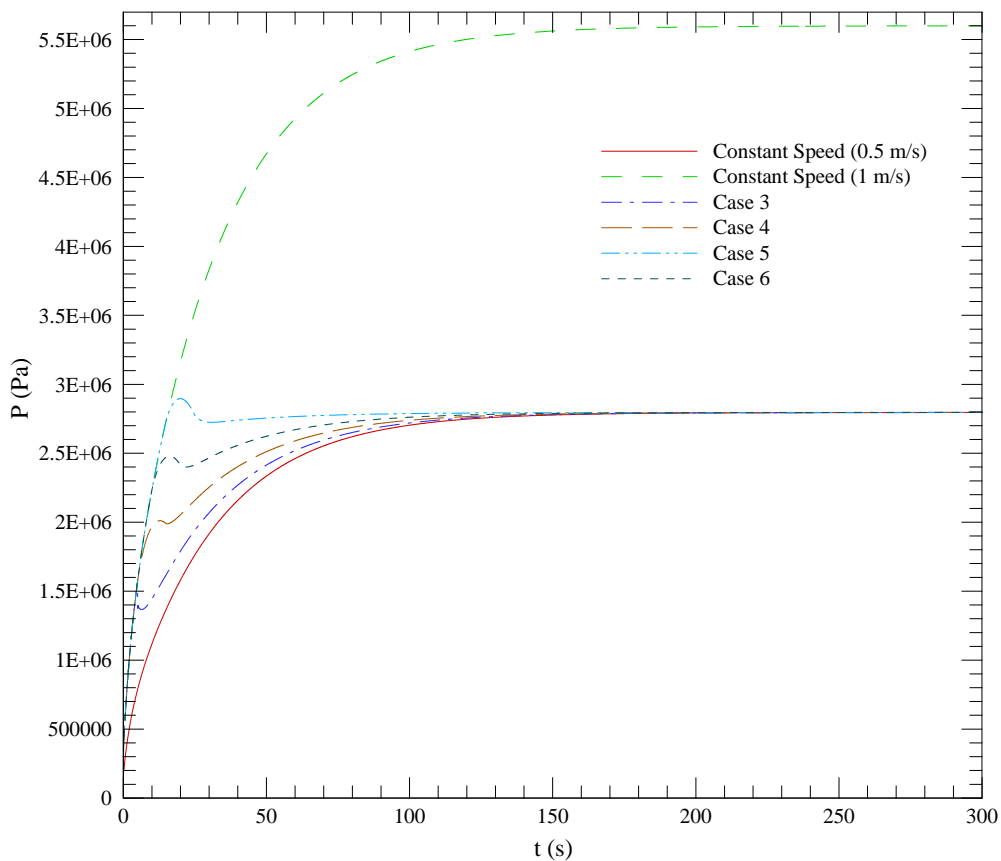The results for the six cases are presented in Figure 17.

Figure 17 – Variations in drillpipe velocity effects in the pressure field

The comparison between the curves for drillpipe velocity of 0.5 and 1.0 m/s shows that the increase in the drillpipe velocity causes an increase in the steady state pressure, due to the greater pressure losses in the second case. When the speed variation is step-like (case 3), the pressure decreases abruptly, because of the sudden drillpipe slowdown. The curves related to the ramp-like speed variation are smoother and have different behavior depending on the time that the ramp starts. When the ramp starts at 15 seconds there is a pressure peak above steady state pressure, and that could cause problems if the pressure was greater then the fracture pressure of the well.

Table 4 show the covered distance for the different situations, considering that the process would last two minutes. From a combined analysis of both Table 4 and Figure 17, it is possible to notice that the period of drillpipe movement can be diminished when the drillpipe speed is varied, and the pressure limits may still be respected.

Table 4 – Covered distances in each case in a 2 min period.

Case	Covered distance [m]
Constant Velocity (0,5 m/s)	60
Case 3	62,5
Case 4	65
Case 5	67,5
Case 6	70

7. CONCLUSION

In this work, a mathematical model to predict surge and swab pressures is presented. The equations of motion are solved numerically by the finite volume method. The unsteady axial Couette flow between concentric surfaces is investigated throughout a parametric analysis. The flow is assumed isothermal with constant compressibility.

An increase of the dimensionless compressibility causes an increase in the pressure at the bottom hole and also on the time for the pressure to reach the steady state. For low compressibilities, the pressure wave motion is clearly observed during the beginning of the simulation.

The time for the steady state to be reached also increases as the aspect ratio increases. For low aspect ratios, the pressure oscillates reaching values larger than the steady state pressure. This oscillation is the result of pressure wave reflections at the boundaries of the domain. The lower the aspect ratio, the higher the amplitude of the pressure peaks.

An interesting phenomenon observed was the flow inversion with time. Viscous drag and pressure gradient make the fluid to flow in opposite directions, and their effects are dominants at different times. In the beginning, viscous drag defines the flow direction. As the time evolves, the pressure gradient effect increases reverting the flow direction with time. It was also noted that the limit for the opposite direction velocity is the Couette velocity for a purely drag driven flow.

It was also noticed that the steady state pressure is directly dependent on the Power Law index. Additionally, if the Power Law index is too small the pressure field oscillates, as the dissipation is smaller.

Finally, six different situations regarding velocity changes were analyzed. It was noticed that such variation may be beneficial, as longer distances are covered in less time and the pressure limits may still be observed.

8. ACKNOWLEDGEMENTS

9. REFERENCES

Anderson, J. D. "Modern Compressible Flow: With Historical Perspective". 2. ed. United States of America: McGraw-Hill, 1990. 650 p.

Bing, Z, Kaiji, Z. and Qiji, Y., 1995, "Equations help calculate surge and swab pressures in inclined well". Oil & Gas Journal, Sep. 18, Vol. 93, p. 74-77

Fontenot, J. E., and Clark, R. K., "An Improved Method for Calculating Swab and Surge Pressures and Circulating Pressures in a Drilling Well", 1974, SPE 4521.

Kimura, H. F., "Transient Mathematical Model for Newtonian Fluid Flow Caused by Axial Drill Pipe Motion. Surge – Swab". Undergraduate monograph, Mechanical Engineering Department, Federal University of Technology Paraná – UTFPR, Curitiba-PR (in Portuguese).

Lal, M. "Surge and Swab Modeling for Dynamic Pressures and Safe Trip Velocities". In: IADC/SPE Drilling Conference, 1983, New Orleans. p. 427-433.

Mitchell, R. F. "Dynamic Surge/Swab Predictions". SPE Drilling Engineering, v. 6, n.4, p. 325-333, set. 1988.

Versteeg, H. K., Malasekera, W., "Computational Fluid Dynamics", 1 ed. London: Prentice Hall, 1995, 257p.

Wang, Y. and Chuckwu, G. A., 1996, "Unsteady Axial Laminar Couette Flow of Power-Law Fluids in a Concentric Annulus", Industrial Engineering and Chemical Research, p 2039-2047, Vol. 35.

White, Frank M. "Mecânica dos Fluidos". 4. ed. Rio de Janeiro: McGraw Hill, 1999. 570 p.

Yang, L. and Chukwu, G. A., 1995, "Couette flow of non-newtonian power-law fluids in narrow eccentric annuli", Industrial Engineering and Chemical Research, p.936-942, Vol. 34.

10. RESPONSIBILITY NOTICE

The authors are the only responsible for the printed material included in this paper.